Efficient rejuvenation of heterogeneous {[(Fe$_{0.5}$Co$_{0.5}$)$_{0.75}$B$_{0.2}$Si$_{0.05}$]$_{96}$Nb$_4$}$_{99.9}$Cu$_{0.1}$ bulk metallic glass upon cryogenic cycling treatment

Siyi Di [a], Qianqian Wang [a], Yiyuan Yang [a], Tao Liang [a], Jing Zhou [a], Lin Su [b], Kuibo Yin [b], Qiaoshi Zeng [a], Litao Sun [b], Baolong Shen [a,c,*]

[a] School of Materials Science and Engineering, Jiangsu Key Laboratory for Advanced Metallic Materials, Southeast University, Nanjing, 211189, China
[b] SEU-FEI Nano-Pico Center, Key Laboratory of MEMS of Ministry of Education, Southeast University, Nanjing, 210096, China
[c] Institute of Massive Amorphous Metal Science, China University of Mining and Technology, Xuzhou, 221116, China

ARTICLE INFO

ABSTRACT

The effects of cryogenic thermal cycling on deformation behaviour and structural variation of {[(Fe$_{0.5}$Co$_{0.5}$)$_{0.75}$B$_{0.2}$Si$_{0.05}$]$_{96}$Nb$_4$}$_{99.9}$Cu$_{0.1}$ bulk metallic glass (BMG) were studied and compared with Cu-free [(Fe$_{0.5}$Co$_{0.5}$)$_{0.75}$B$_{0.2}$Si$_{0.05}$]$_{96}$Nb$_4$ BMG. After thermal-cycled treatment between 393 K and cryogenic temperature, the {[(Fe$_{0.5}$Co$_{0.5}$)$_{0.75}$B$_{0.2}$Si$_{0.05}$]$_{96}$Nb$_4$}$_{99.9}$Cu$_{0.1}$ BMG obtained a plastic strain of 7.4% combined with a high yield strength of 4350 MPa. The excellent soft magnetic properties were maintained after CTC treatment. The minor addition of Cu element results in an initial nano-sized heterogeneity in the matrix, which facilitates the rejuvenation process during thermal cycling, and brings to a low optimal thermal temperature of 393 K, making the {[(Fe$_{0.5}$Co$_{0.5}$)$_{0.75}$B$_{0.2}$Si$_{0.05}$]$_{96}$Nb$_4$}$_{99.9}$Cu$_{0.1}$ BMG more attractive in industrial application. During thermal cycling, the formation of more soft regions leads to the increase of structural heterogeneities, which is beneficial to the initiation of shear transition zones and the formation of multiple shear bands, and thus results in the enhancement of plasticity. This study links the subtle variation of specific structure with macroscopic mechanical properties, and provides a new insight of composition selection for cryogenic thermal cycling treatment.

© 2021 Published by Elsevier Ltd on behalf of Chinese Society for Metals.

1. Introduction

Since the first synthesis of Fe-based bulk metallic glass (BMG) in 1995 [1], they have attracted intense attention for applications as structural and functional materials because of their excellent soft-magnetic properties and ultra-high strength, combined with low raw material cost [2,3]. However, room-temperature brittleness of most Fe-based BMGs severely restricts their engineering applications [3,4]. In the past decades, great efforts have been devoted to develop ductile Fe-based BMGs. For those BMGs with large plastic strain, researchers have linked their superior plasticity with distinct nano-scale heterogeneities within the BMG matrix [5,6]. In principle, the plasticity of metallic glass (MG) is precisely attributed to the response of the heterogeneous amorphous structure to external mechanical stimuli. The increase of nano-scale heterogeneities in MGs generally results in activation of more shear transition zones (STZs), and sometimes induces propagation obstacles for shear bands (SBs) during the plastic flow, thus improving

the plasticity of MGs [6,7]. This recognition sheds some light on the plastic strain improvement for Fe-based BMGs.

Recently, a new method called cryogenic thermal cycling (CTC) has been proved effective to improve the plasticity by magnifying intrinsic structural heterogeneity in MGs [8]. With suitable process parameters (temperature, cycle index and so on), some MGs can reach a more rejuvenated state with increased structural heterogeneities. Comparing with some mechanical approaches to realize rejuvenation, such as the high pressure torsion and shot peening, this thermal approach has no limitation on sample size and works across the whole sample. Particularly, it is barely detrimental to the soft-magnetic properties of the Fe-based MGs [9].

Due to the obvious superiority of CTC treatment, a series of BMGs have been processed using this method. Significant rejuvenation effects on mechanical properties (improved compressive plasticity, and reversal of annealing-induced embrittlement) have been achieved in some systems [8–10]. However, some BMGs had no response and even underwent inferior plasticity after CTC treatment [11] and the reason has not yet been clarified. Besides, the initial degree of structural heterogeneity before CTC treatment

* Corresponding author.

seems to play an important role. It has been reported that more heterogeneous MGs (e.g. MG-matrix composites with dispersed crystallites [12], MGs containing nano-sized clusters [13], and MGs with chemical inhomogeneity [14]) are more affected by CTC treatment than homogeneous MGs. However, the atomic-scale mechanism has not been clarified, and it remains unclear whether it is suitable to different MG systems. To make CTC treatment effectively applied, it is of great importance to clarify the relationship between subtle structural change and the mechanical response to CTC treatment. Meanwhile, a correlation between the initial structure of MGs and the final state after CTC treatment is imperative to be established.

In previous study, the CTC treatment has been proved an effective measure to rejuvenate the $[(Fe_{0.5}Co_{0.5})_{0.75}B_{0.2}Si_{0.05}]_{96}Nb_4$ (note BA_{100} hereafter) BMG samples and significantly improve its plasticity [15]. Herein, with minor addition of 0.1 at.% Cu, which has a positive enthalpy with Fe element, a relatively more heterogeneous structure can be achieved in the $\{[(Fe_{0.5}Co_{0.5})_{0.75}B_{0.2}Si_{0.05}]_{96}Nb_4\}_{99.9}Cu_{0.1}$ (note $BA_{99.9}Cu_{0.1}$ hereafter) BMG. The effect of CTC treatment on this BMG has been carefully studied to explore the influence of initial structure. A significantly improved plastic strain (ε_p) of 7.4% combined with a super-high yield strength (σ_y) over 4300 MPa were obtained when the thermal temperature was 393K, far below that for BA_{100} BMG. The excellent soft magnetic properties were maintained after CTC treatment. The initial nano-scale heterogeneities induced by Cu addition facilitate the formation of internal stress at a much lower thermal temperature, leading to a rejuvenated state with increased amount of loosely packed regions. Besides, it is interesting to find that some of the preexisting crystal-like orderings (CLOs) were destructed after thermal cycling, indicating another disordering process.

2. Experimental

2.1. Sample preparation

Alloy ingots with a nominal atomic composition of $\{[(Fe_{0.5}Co_{0.5})_{0.75}B_{0.2}Si_{0.05}]_{96}Nb_4\}_{99.9}Cu_{0.1}$ were prepared by induction melting a mixture of high-purity (>99.9 wt.%) constituent elements in a highly purified argon atmosphere. Cylindrical BMG samples with a diameter of 1 mm were produced by copper mold casting. Subsequently, the as-cast $BA_{99.9}Cu_{0.1}$ BMG samples were subjected to CTC treatment for 15 cycles, and each cycle consists of dipping the sample into liquid nitrogen for 1 min and then high-temperature silicone oil (Polydimethylsiloxane, supplied by Dow Corning) for 1 min. The thermal temperatures are 353, 373, 393, 433, and 473 K (0.43-0.58 of the glass transition temperature, T_g). The as-cast sample and CTC treated samples at different oil temperatures are denoted as AC, CTC353K, CTC373K, CTC393K, CTC433K, and CTC473K samples, respectively.

2.2. Sample characterization

The phase compositions of the samples were investigated by X-ray diffraction (XRD, D8-Discover, Bruker) with Cu-Kα radiation. Mechanical properties of the samples were measured at room temperature by compression tests using a Sans 5305 electromechanical testing machine with a strain rate of 5×10^{-4} s^{-1}. The AC and CTC treated samples for the compression tests had 2:1 aspect ratios (1 mm in diameter and 2 mm in height), and 10 samples for each condition were conducted to ensure the repeatability. The lateral surface morphology prior to fracture and morphology of fracture surface were analyzed by scanning electron microscopy (SEM, Sirion 200, FEI). The saturation magnetic flux density (B_s) was measured with a vibrating sample magnetometer (VSM, Lake
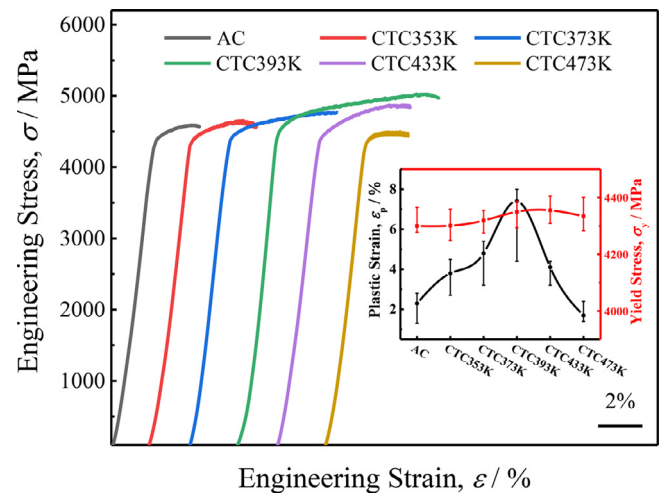

Fig. 1. Representative engineering stress-strain curves of the AC and CTC treated $BA_{99.9}Cu_{0.1}$ BMG samples. Inset shows the values of σ_y and ε_p with error bars.

Shore 7410) under an applied field of 400 kA/m, the coercivity (H_c) was measured with a B-H loop tracer (RIKEN BHS-40) under a field of 1 kA/m and the effective permeability (μ_e) was measured by an impedance analyzer (E4990A) under a field of 1 A/m. The enthalpy of relaxation (ΔH_{rel}) was measured by differential scanning calorimeter (DSC, Netzsch 404 F3) to evaluate the degree of rejuvenation for AC and CTC treated samples. The samples were heated from 313 K to 973 K (above T_g) at a heating rate of 20 K/min, and then cooled to 313 K, followed by a second cycle using the same procedure. The ΔH_{rel} is calculated from the area between the first and second cycle curves, from the onset of relaxation to T_g. 5 samples for each condition were tested to assess the repeatability of ΔH_{rel} measurements. Synchrotron XRD analysis was conducted to examine the total structural change using the high-energy monochromatic beam with wavelength of 0.6199 Å at Sector 15U1 of the Shanghai Synchrotron Radiation Facility. The two dimensional diffraction images were recorded using a Perkin-Elmer amorphous silicon detector and integrated using the Fit2D program to obtain 1D intensity distributions as a function of the wave vector. High-resolution transmission electron microscopy (HRTEM) analysis of the bulk rods before and after thermal cycling was carried out on an aberration-corrected FEI Titan 80-300 transmission electronic microscope to observe the subtle microstructural changes. The samples for HRTEM analysis were thinned by ion milling method (Gatan Inc., PIPS-M691) under liquid nitrogen cooling condition. The nano-indentation tests were performed to verify the structure heterogeneity using a NanoTest Vantage (Micro Materials Ltd) under load control model. The loading and unloading rates were 1 mN s^{-1}. The maximum load (F_{max}) was 50 mN and the holding time at the F_{max} is 20 s. A diamond spherical indenter with a tip radius 5 μm was used.

3. Results

3.1. Effects of CTC treatment on mechanical behavior

The typical engineering stress-strain curves of the AC and CTC treated $BA_{99.9}Cu_{0.1}$ BMGs are shown in Fig. 1, and the inset is the variation tendency of σ_y and ε_p with error bars. Manufacturing flaws, such as the inclusions and surface irregularities cannot be avoided during material fabrication. These flaws can serve as facilitators to the process of runaway shear failure since BMGs are flaw sensitive. Besides, the possibly local fluctuations in the chemistry or density (free volume) of the glass structure itself exert a large
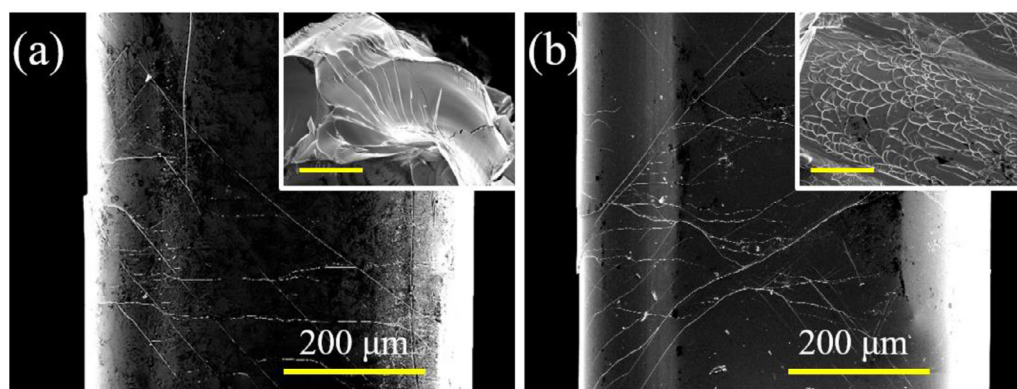
Fig. 2. SEM images of lateral surface for the deformed (a) AC and (b) CTC393K samples for $BA_{99.9}Cu_{0.1}$ BMG. Insets in (a) and (b) show fracture surface of the corresponding samples (scale bars - 100μm).

influence on rejuvenation degree [16]. Thus, the error of ε_p is relatively large. Nevertheless, it is obvious that the ε_p increases with the CTC temperature increasing from 353 to 393 K, then decreases with further increasing CTC temperature to 433 and 473 K. After CTC treatment with different thermal temperatures, the compressive plasticity can be improved to different extent, except that the CTC473K sample has a plastic strain ($\varepsilon_p = 1.7\%$) even below that of AC sample ($\varepsilon_p = 2.3\%$). Despite the ε_p shows variable response to the different thermal temperatures, the σ_y remains almost unchanged and above 4200 MPa. As a result, a FeCo-based BMG with ε_p of 7.4% and ultra-high σ_y of 4350 MPa is achieved through CTC treatment when the thermal temperature is 393K.

The lateral surface morphology prior to fracture of the AC and CTC393K samples are shown in Fig. 2, and the morphology of fracture surface are shown in the insets. For the AC sample (Fig. 2(a)), although there appear to be several shear planes, SBs cross through the sample with little branching, causing immediate failure. While for the CTC393K sample (Fig. 2(b)), multiple SBs with all sorts of directions can be observed, and the intersections of SBs are much more abundant than that in the AC sample. Generally, the global plasticity of BMGs is determined predominantly by the amount of SBs generated during compression test [17]. This explains the larger ε_p in CTC393K sample. Besides, in AC sample, most areas of the fracture surface are glossy and exhibit cleavage-like structure, combined with river-like cracks. This behavior is usually observed on the fracture surface of brittle BMGs and is associated with fast fracture because of the rapid propagation of SBs [18]. The vein pattern morphology is only observed at the edge of the rod, suggesting that local heating accompanies shear during mechanical failure [19]. While the CTC393K sample exhibits a well-developed vein pattern, which is usually observed in the non-ferrous BMGs with good ductility. The characteristic vein pattern indicating that the SB has higher stability during its propagation in the CTC393K sample, which is another evidence of brittle to ductile transformation.

3.2. Effects of CTC treatment on magnetic properties

The magnetic properties before and after CTC treatment were measured and shown in Fig. 3. It is worth noting that when we talk about the magnetic properties of Fe-based MGs, we often refer to the sample that treated with stress relieving annealing. Therefore, we annealed the as-cast samples at 755 K (55 K below T_g) for 20 min firstly (noted as 755K), and then treated them with CTC at 393 K (noted as 755K-CTC393K). Afterwards, the B_s, H_c and μ_e of the annealed samples before and after CTC treatment were measured. Fig. 3 shows the B-H curves for the two samples with partly enlarged drawing in the inset. The B_s is 1.05 T for both the 755K
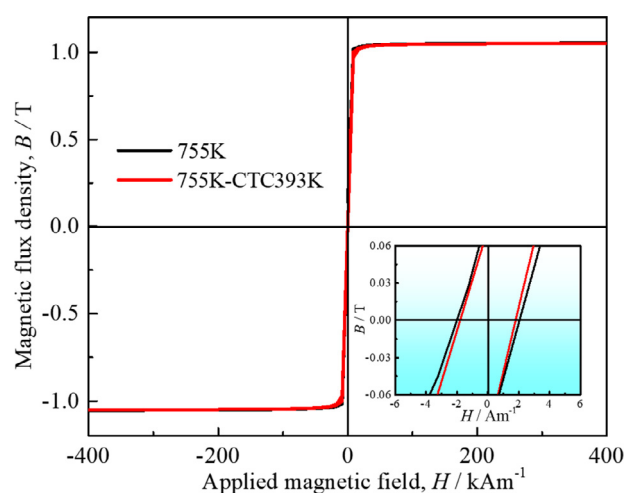

Fig. 3. B-H curves of the 755K sample and 755K-CTC393K sample with partly enlarged drawing in the inset.

and 755K-CTC393K samples, the H_c is 2.0 A/m for the 755K sample and 1.8 A/m for the 755K-CTC393K sample. Besides, μ_e at 1 kHz is 13700 for the 755K sample and 13400 for the 755K-CTC393K sample. The differences of magnetic properties before and after CTC treatment are within the range of measurement error. Besides, we also measured the magnetic properties of the AC and CTC393K samples without stress relieving annealing, and no noticeable difference in the magnetic properties is observed either. The above results indicate that the excellent soft magnetic properties are maintained after CTC treatment.

3.3. Effects of CTC treatment on thermal properties

Because the CTC process is generally associated with the change of stored energy, the relaxation state of the samples before and after CTC treatment was carefully studied. Fig. 4(a) shows the typical relaxation spectra of the AC and CTC treated samples, and the ΔH_{rel} before T_g is represented by the dashed area below the horizontal lines. Fig. 4(b) shows the values of ΔH_{rel} for the AC and CTC treated samples, and the error bars are calculated from 5 repeated tests. It can be seen that the ΔH_{rel} increases from 0.443 KJ mol^{-1} for the AC sample to 0.618 KJ mol^{-1} for the CTC433K sample, and then decreases to 0.589 KJ mol^{-1} for the CTC473K sample. The exothermic heat of relaxation is associated with relaxation state and closely related to total fraction of free volume in MG [20]. In general, a higher ΔH_{rel} means a more rejuvenated state and ad-
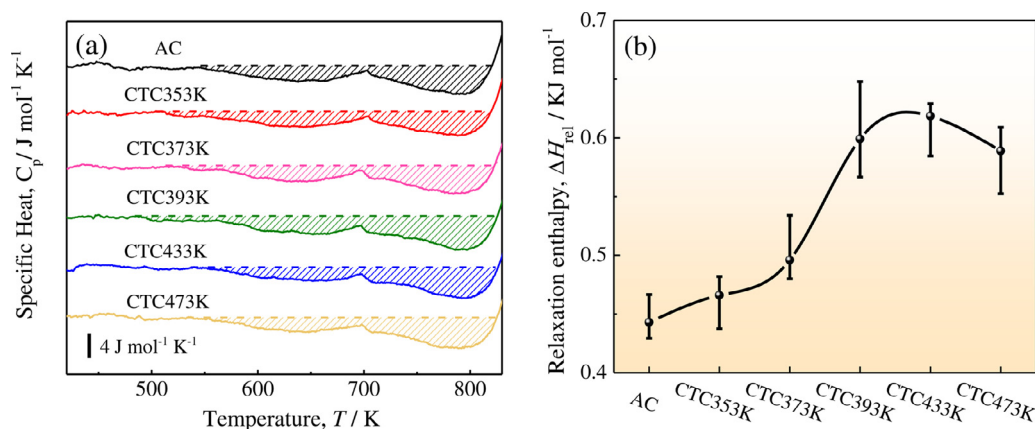
Fig. 4. (a) Typical relaxation spectra and (b) variation of ΔH_{rel} with error bars for the AC and CTC treated $BA_{99.9}Cu_{0.1}$ BMG samples.
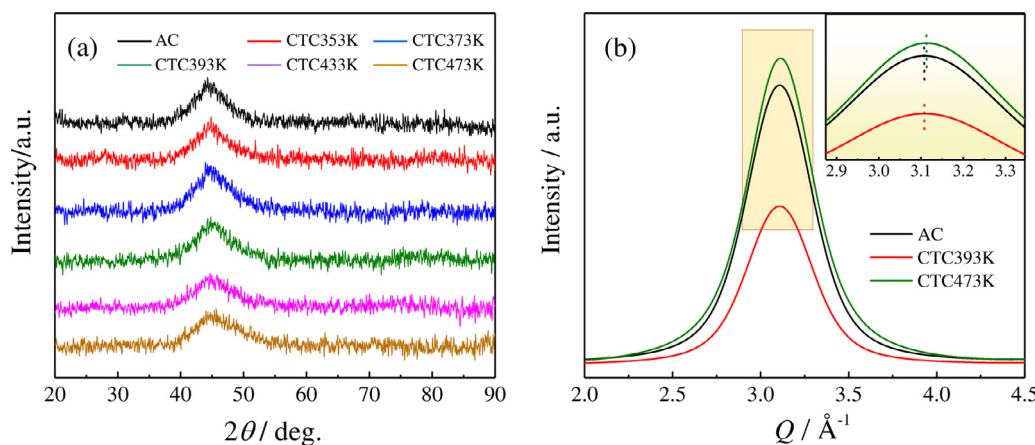

Fig. 5. (a) XRD patterns of the AC and CTC treated $BA_{99.9}Cu_{0.1}$ BMG samples. (b) Synchrotron XRD patterns of AC, CTC393K, and CTC473K samples. Inset is the magnification image of the yellow rectangular area.

ditional free volume. The regions containing larger amount of free volume have lower local stiffness and stability, and are often referred to as liquid-like regions [21] when structural heterogeneity is considered. These soft regions provide fertile sites for SB initiation, leading to a superior plastic deformation capacity in MG [22]. Nevertheless, after CTC treatment, the value of ΔH_{rel} demonstrates an inconsistence with ε_p. Although the CTC393K sample has similar ΔH_{rel} with CTC473K sample, the ε_p of the two samples are radically different. This behaviour is also found in the BA_{100} BMG and other BMGs that have been reported [10,15]. It maybe because that the thermodynamic properties predominately reflect average changes in the structure while the plasticity is predominantly affected by only a small fraction of atoms undergoing large re-arrangements [23].

3.4. Effects of CTC treatment on multi-scale structure

The phases of the samples were investigated by XRD measurements and all samples keep amorphous structure after CTC treatment, as can be seen in Fig. 5(a). Furthermore, a more refined examination for atomic-scale structural changes for the AC, CTC393K, and CTC473K samples were carried out by Synchrotron XRD (Fig. 5(b)). The smooth curves without sharp diffraction peaks confirm the normal XRD results. Besides, it is obvious that the CTC473K sample shows the strongest normalized intensity, followed by the AC, and then the CTC393K sample. The lower intensity in the Synchrotron XRD often indicates a more disordered structure, which leads to a superior plasticity [24]. The Synchrotron

XRD result is consistent with the plastic performance of the BMGs. Furthermore, the encircled part of the diffraction peaks is shown in the inset for clarity, with the dashed lines denoting their peak positions (Q). The diffraction peak of the AC sample locates at a Q value of 3.109 $Å^{-1}$, and that for CTC393K and CTC473K samples is 3.108 $Å^{-1}$ and 3.113 $Å^{-1}$, respectively. Because there is an inverse correlation between the diffraction peak position Q value and average interatomic spacing of MG [25], the increase of Q value for the CTC473K sample indicates a 0.129% decrease in average interatomic spacing and 0.387% increase in volume density, indicating a more densely packed structure. For the CTC393K sample, the change is only 0.096% increase in average interatomic spacing. Even though the effect of thermal cycling on the local regions might be very large, the effect on average interatomic spacing is relatively small due to their small volume fraction.

The nano-scale structural information is examined by aberration-corrected HRTEM. Fig. 6(a–c) are the HRTEM images for the AC, CTC393K and CTC473K samples, with the corresponding selected area electron diffraction (SAED) patterns shown in the insets. The diffuse halo rings of SAED patterns confirm the amorphous structure of the samples before and after thermal cycling, while the atomic-scale structure of the three samples differs a lot. As shown in Fig. 6(a), a large amount of CLO structures with a size around 1 nm can be observed. The lattice fringe spacing includes 1.99 ± 0.05 Å for (110) lattice space of α-Fe crystalline phase, as well as 1.90 ± 0.05 Å, 2.15 ± 0.05 Å and 2.09 ± 0.05 Å (not shown in the picture) for (440), (422) and (511) lattice spaces of $Fe_{23}B_6$ crystalline phase. It is worth noting that, the
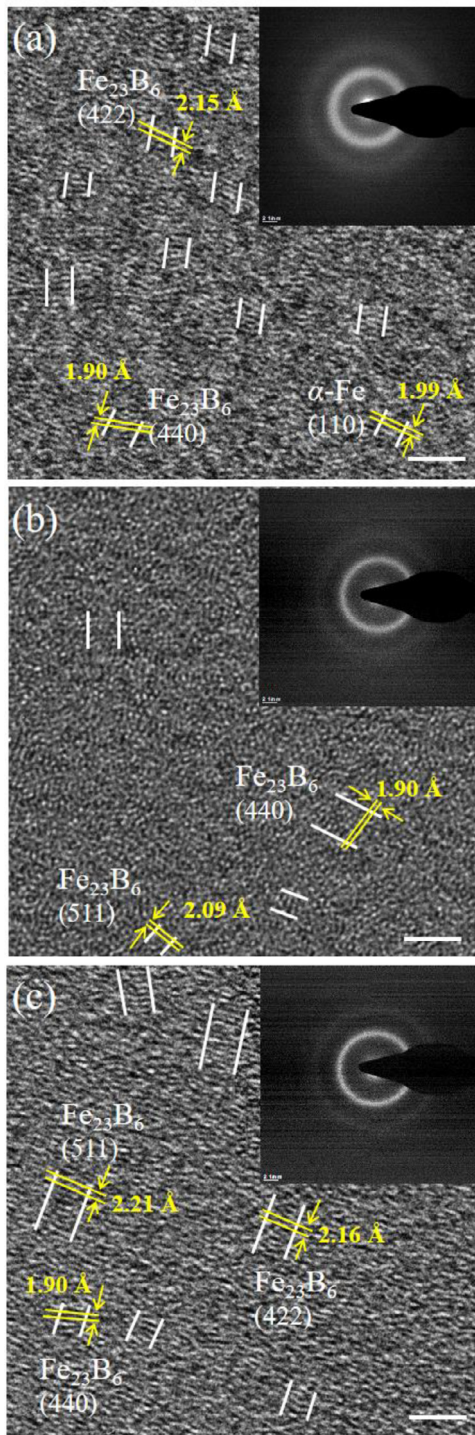
Fig. 6. HRTEM images with the corresponding SAED patterns as insets for BA$_{99.9}$Cu$_{0.1}$ BMG samples of (a) AC, (b) CTC393K, and (c) CTC473K. The white lines highlight the CLO/NC structures (scale bars - 2 nm).

initial precipitation phase for the BA$_{100}$ BMG is Fe$_{23}$B$_6$ [15,26], while with minor addition of Cu element, the as-cast BA$_{99.9}$Cu$_{0.1}$ BMG possesses two types of CLO structures. The coexistence of α-(Fe,Co) and (Fe,Co)$_{23}$B$_6$ microcrystalline grains is also found in {[(Fe$_{0.5}$Co$_{0.5}$)$_{0.75}$B$_{0.2}$Si$_{0.05}$]$_{96}$Nb$_4$}$_{99.75}$Cu$_{0.25}$ bulk glassy alloy composite [27]. This is because that the mixing enthalpy of Fe–Cu atomic pair is +13 J/mol, the Cu clusters can form in the amorphous matrix prior to the onset of crystallization. When Cu clusters form, Fe atoms are rejected from the Cu clusters and

would pile-up at the Cu/amorphous matrix interface. Besides, there are lattice orientation relationships between the Cu particles and the α-Fe primary crystals, i.e., Nishiyama-Wassermann and Kurdjumov-Sachs orientation relationships [28]. As a result, the Cu clusters can serve as heterogeneous nucleation sites for α-Fe, which is beneficial to the precipitation of α-Fe phase. According to the quantitative analysis, more than half of the CLOs possess α-Fe structure. For the CTC393K sample (Fig. 6(b)), it is interesting to find that most of the CLO structures disappear, leaving a significantly disordered matrix with only a few CLO structures. This is consist with the synchrotron XRD result that the CTC393K sample has a more disordered structure. The remaining ones also have a size around 1 nm but only have lattice fringe spacing of 1.90 $\pm$ 0.05 Å and 2.09 $\pm$ 0.05 Å, corresponding to the Fe$_{23}$B$_6$ crystalline phase. There are two explanations for this phenomenon. One is that CLOs with α-Fe structure are all destructed and some CLOs with Fe$_{23}$B$_6$ structure remained. Ferromagnetic amorphous alloy has an Invar effect below Curie temperature (700 K in this paper), resulting in spontaneous volume magnetostriction and thus a smaller thermal expansion coefficient compared to its crystalline phase [29]. Therefore, CLOs with crystal-like structures are affected more by thermal stress compared to the amorphous structure and are inclined to be destroyed during the expansion and contraction process. The destruction of CLOs has also been observed during annealing in MGs [30], which confirms that the CLO structure is not very stable. This situation is more applicable to the CLOs with α-Fe structure because the Fe$_{23}$B$_6$ structure is more rigid thus influenced little to certain thermal stress. Another explanation of the partly remained CLOs of Fe$_{23}$B$_6$ structure is that along with the complete decomposition of pre-existing CLO structures, some new CLOs with Fe$_{23}$B$_6$ structure can form in other regions, because the internal stress not only brings to disordering but also local relaxation and even crystallization [13,15]. The existence of CLOs with a size of ~1 nm has been reported in other BMGs, and has been considered to be beneficial to plasticity [6,31]. Local structural heterogeneity increases due to these highly-ordered clusters, which constitutes the main resistance for plastic flow in BMGs. For the CTC473K sample (Fig. 6(c)), the CLOs with Fe$_{23}$B$_6$ structure has a size of 2-3 nm, taking up vast space. This may illustrate the distinct decrease in average interatomic spacing for the CTC473K sample. The observed larger Fe$_{23}$B$_6$ nanocrystals (NCs) are considered to grow up from the CLOs with Fe$_{23}$B$_6$ structure which retained or formed during thermal cycling according to the above discussion. And the crystal formation has been confirmed to be irrelevant to the thermal temperature but the internal stress because of the wide temperature differential in the previous study [15]. The growing up Fe$_{23}$B$_6$ nanocrystals are hard and brittle, stress concentration often occurs around these regions, and numerous STZ clusters generate in a certain narrow belt and quickly form a macroscopic crack [32]. This may illustrate why the CTC473K sample possesses an inferior plasticity.

Nano-indentation tests were carried out to investigate the microscale structural heterogeneities after thermal cycling. In nano-indentation test, the loading discontinuities can be linked directly to the initiation of individual SB, thus it helps to reveal the deformation mechanism [33]. Fig. 7(a) is a representative load-displacement (P–h) curve for the AC sample, and the initial yield event (pop-in) is marked by a discrete displacement burst. The first pop-ins are characterized by the values of initial yield load F_y and initial yield displacement Δh, and the initial yield pressure P_y is calculated from [34]:

$$P_y = F_y/A = F_y/(2\pi R h_c)$$

where A is contact area, R is the indenter tip radius, h_c is the contact depth at initial yield calculated according to the reference [34]. P_y stands for the strength required for the initiation of plas-
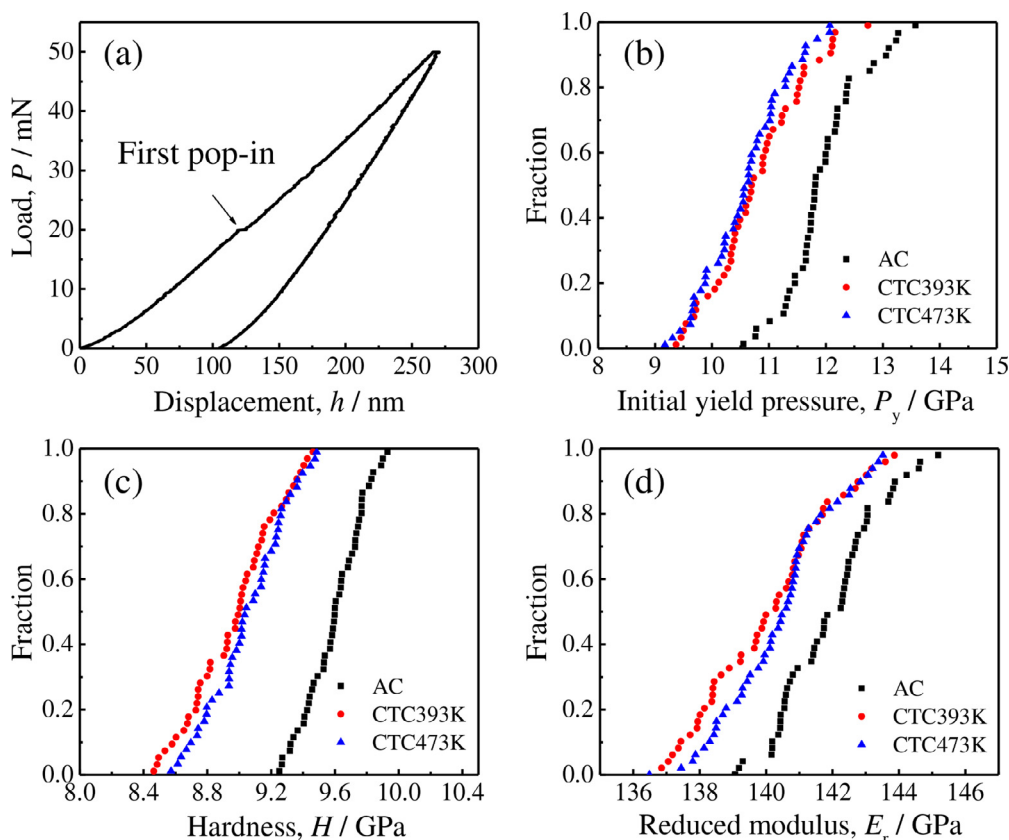
Fig. 7. (a) A representative nano-indentation load-displacement curve of the AC sample. Cumulative distributions of (b) P_y, (c) H and (d) E_r for the AC, CTC393K and CTC473K samples.

tic flow. The cumulative distribution of P_y for the AC, CTC393K and CTC473K samples are compiled from 49 loading curves. By getting rid of some curves without distinct pop-in behaviour, 44 to 48 data points are included for each distribution curve (Fig. 7(b)). It is obvious that after thermal cycling, the P_y of the samples decreases to lower values. The median value of P_y is 11.82 GPa for AC sample, 10.70 GPa for CTC393K sample and 10.60 GPa for CTC473K sample. Thus, the initiation of SB is easier in CTC393K and CTC473K samples than in AC sample, indicating more soft regions are induced after thermal cycling. Besides, the relative width (1st to 9th decile, relative to the median value) of the P_y distribution is 7.6% for AC sample, 11.3% for CTC393K sample and 9.4% for CTC473K sample, suggesting that cycling induces greater heterogeneity in the structure [8]. The hardness H and reduced elastic modulus E_r is determined by the standard Oliver and Pharr method [35]. Similar with P_y, the cumulative distributions of H and E_r for the three samples are shown in Fig. 7(c) and (d). The AC sample has the largest H with the median value of 9.60 GPa, followed by 9.04 GPa for CTC473K sample and 8.99 GPa for CTC393K sample. The relative width is 3.2% for AC sample, 5.1% for CTC393K sample and 4.5% for CTC473K sample. The E_r shows similar behaviour to H. The median value of E_r decreases from 142.25 GPa for the AC sample to 140.58 GPa for CTC473K sample and 140.02 GPa for CTC393K sample. After cycling treatment the relative width of the E_r distribution increases from 3.4% for AC sample to 3.8% for CTC473K sample and 4.4% for CTC393K sample. Because the loosely-packed regions possess lower modulus and hardness, the reduced H and E_r also prove structural softening after thermal cycling. Besides, the largest relative width of the CTC393K sample indicates highest heterogeneity in the structure. It worth noted that the relative width of H and E_r is much smaller than P_y. This is because that

P_y is related to the initiation of plastic flow, so that is sensitive to the local soft regions, while H and E_r reflect the matrix of the MG, thus is less sensitive to the heterogeneous local structure. This may also illustrate why the CTC473K sample possesses lower P_y but higher H and E_r compared with the CTC393K sample. Although the CTC473K sample has more soft regions indicated by its lower P_y, the increased hard nanocrystals with 2-3 nm leads to higher hardness and modulus. The loosely-packed regions are easier to be activated and promote the nucleation of STZs during the redirection of SBs/microcracks in a percolated network structure, which contributes to a preferred plastic deformation in the CTC393K sample. While for the CTC473K sample, although the quantity of soft regions is larger than the CTC393K sample, the inferior plasticity is mainly attributed to the brittle nanocrystals with a size of 2-3 nm.

4. Discussion

4.1. Origin of plasticity enhancement after thermal cycling

According to the nano-indentation results, thermal cycling can induce more soft regions in both CTC393K and CTC473K sample, which facilitate the activation of STZs and the initiation of SBs. However, a high temperature during thermal cycling may also induce local relaxation and ordering, and even crystallization, for example, in CTC473K sample. It is proposed that amorphous structure specifically comprises three discernible regions: liquid-like, transition, and solid-like regions, with different atomic performance to external agitations [36]. The liquid-like regions has loosely packed local configuration, corresponding to the soft regions, where the anelastic atoms are easier to be activated. The
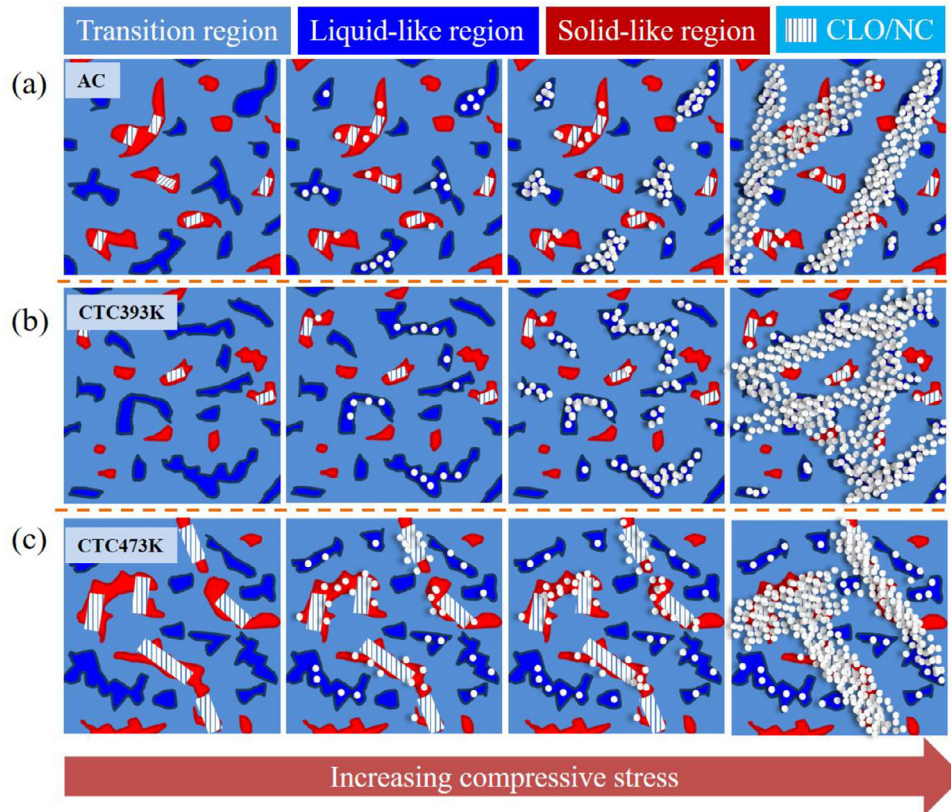
Fig. 8. Schematic illustration for atomic response to mechanical agitations before global yielding during compression for (a) AC, (b) CTC393K and (c) CTC473K samples for $BA_{99.9}Cu_{0.1}$ BMG.

solid-like regions are composed of densely packed atoms, including local orderings and even nanocrystals in this case. The transition regions serve as an intermediary between the contrasting characteristics of the solid-like and liquid-like regions. Fig. 8 (a–c) show the schematic illustration for different atomic response to mechanical agitations before global yielding during compression for AC, CTC393K and CTC473K samples because of their different amorphous structure. The light blue regions represent transition regions, the dark blue regions represent liquid-like regions, while the red regions represent solid-like regions, with CLO/NC (white rectangles with lines) included. The white spheres denote the locations of anelastic atoms prior to global yielding under loading. The direction of arrow denotes the magnitude of compressive stress. In general, the localization strain during deformation includes the nucleation and percolation of STZs, followed by the initiation and propagation of SBs [37]. For the AC sample, the proportion of liquid-like regions is relatively low, revealed by its small ΔH_{rel} and high P_y. CLOs of $Fe_{23}B_6$ and α-Fe structures with size of 1nm disperse in the matrix. These CLOs won't cause significant stress concentration because of their small size. Instead, they can serve as obstacles to hinder the propagation of primary SBs. However, although the CLOs may facilitate the branching and intersection of SBs, because of the limited soft regions, the nucleation and percolation of STZs tend to be difficult and the total number of SBs penetrating through the sample is relatively small, which results in intense degree of strain localization and failure at a smaller plastic strain. For the CTC393K sample, it has the highest structural disordering because of a large fraction of loosely packed regions. CLOs of $Fe_{23}B_6$ structure contribute to the solid-like regions. The soft regions are fertile sites for STZs nucleation and SBs initiation. And the latter propagation of SBs is impeded by the relatively stronger

transition regions and solid-like regions, leading to a stable shearing process. The massively activated SBs hinder and intersect with each other during propagation, leading to the formation of multiple SBs and energy release, thus an improved plasticity. The improvement of plasticity of CTC393K sample is considered as a combination effect of CLOs with size of 1 nm and increased soft regions. While for the CTC473K sample, although it has higher ΔH_{rel} compared to the CTC393K sample, which indicates that the number of liquid-like regions is larger, the CTC473K sample has much inferior plasticity, even worse than the AC sample. In this case, the decreased plasticity probably associates with the 2-3 nm $Fe_{23}B_6$ crystalline structures. In some cases, the crystalline reinforcements are considered as source and sink for the STZs and thus are beneficial to the formation of multiple SBs [6,38]. However, the crystalline structures may also deteriorate the macroscopic plasticity due to their type, distribution, and quantity. For the $BA_{99.9}Cu_{0.1}$ BMG, the large and brittle $Fe_{23}B_6$ nanocrystals in CTC473K sample mainly brings stress concentration and leads to a rapid increase of temperature in the vicinity [39], this may result in drastic local shear-softening and critical cavitation. On the intervention of cavitation, plastic shearing is terminated and mechanical energy is dissipated through crack extension [40], resulting in rapid shear-off and failure. Therefore, the stable evolution from SB to crack and the resistance for shear expansion in the deformation process for BMG sample is of equal importance. According to the different plasticity responses of the three samples to the atomic-scale structures, it can be concluded that both the rejuvenation degree and CLOs/NCs play an important role in plasticity. Our results suggest that the effect of thermal cycling on the structure and properties of BMGs is determined by multiple factors and their relative contributions.

4.2. Comparison of CTC treatment on BA_{100} and $BA_{99.9}Cu_{0.1}$ BMGs

Although the thermal cycling is beneficial to both BA_{100} and $BA_{99.9}Cu_{0.1}$ BMGs, the optimal thermal temperature for the two alloys differs a lot, 393 K for $BA_{99.9}Cu_{0.1}$ BMG and 513 K for BA_{100} BMG. This makes the former one more attractive for application when considering energy conservation.

In previous studies, it has been suggested that the rejuvenation process is caused by local stress during thermal cycling [8,11,13]. Such contribution may potentially be the local variation in thermal expansion coefficient which can be considered as the amplitude of the excitation during thermal cycling [41]. In this study, the disappearance of CLOs with α-Fe and $Fe_{23}B_6$ structures confirms this suggestion. According to the HRTEM results and ΔH_{rel} calculation in reference [15], the AC sample of BA_{100} BMG possesses a relatively homogeneous amorphous phase with limited amount of CLO structures and small ΔH_{rel} (0.371 KJ mol^{-1}), thus a larger temperature difference is needed to generate atomic rearrangement during thermal cycling. On the contrast, the AC sample of $BA_{99.9}Cu_{0.1}$ BMG is much more heterogeneous with nano-sized CLO structures and a larger ΔH_{rel} (0.443 KJ mol^{-1}), which should help inducing a larger local stress because of the intrinsic difference between the matrix, CLO structures and soft regions. Meanwhile, because of the smaller temperature differential, the degree of rejuvenation obtained for $BA_{99.9}Cu_{0.1}$ BMG is much lower than BA_{100} BMG after CTC treatment. The difference of ΔH_{rel} between the AC and CTC393K sample for $BA_{99.9}Cu_{0.1}$ BMG is 0.156 KJ mol^{-1}, while for BA_{100} BMG, the difference of ΔH_{rel} between the AC and CTC513K sample is up to 0.306 KJ mol^{-1}. The changes of average interatomic spacing also confirmed this conclusion. The variation of average interatomic spacing is 0.130% for the AC and CTC513K sample for BA_{100} BMG [15] and only 0.096% for the AC and CTC393K sample for $BA_{99.9}Cu_{0.1}$ BMG.

When only considering the degree of rejuvenation after thermal cycling, the ΔH_{rel} is 0.599 KJ mol^{-1} for CTC393K sample of $BA_{99.9}Cu_{0.1}$ BMG and 0.677 KJ mol^{-1} for CTC513K sample of BA_{100} BMG, the Q value is 3.108 Å^{-1} for CTC393K sample of $BA_{99.9}Cu_{0.1}$ BMG and 3.106 Å^{-1} for CTC513K sample of BA_{100} BMG, as a result, the rejuvenation degree of BA_{100} sample is higher than $BA_{99.9}Cu_{0.1}$ sample. However, after thermal cycling, the plasticity of $BA_{99.9}Cu_{0.1}$ BMG (7.4%) is superior to the BA_{100} BMG (6.1%). This result further confirms that the rejuvenation degree after thermal cycling is not the only factor affecting the global plasticity. Even though a net increase in potential energy is observed, rejuvenation and relaxation may occur simultaneously [13,15,41], and the ordered structures can play an important role in plasticity. Besides, the occurrence of rejuvenated regions may be quite different in size, quantity and distribution within the glass. Further studies with more BMG systems and elaborate structural examination should be carried out to reveal the refined structural variation at atomic-scale during thermal cycling and establish a relationship with the plasticity of BMGs.

5. Conclusions

In the present study, the $\{[(Fe_{0.5}Co_{0.5})_{0.75}B_{0.2}Si_{0.05}]_{96}Nb_4\}_{99.9}Cu_{0.1}$ BMG sample obtained a ε_p of 7.4%, ultra-high σ_y of 4350 MPa and maintained excellent soft magnetic properties after CTC treatment. Compared with the Cu-free $[(Fe_{0.5}Co_{0.5})_{0.75}B_{0.2}Si_{0.05}]_{96}Nb_4$ BMG, the optimal thermal temperature decreased sharply from 513 K to 393 K, making the alloy in this study more suitable for industrial production. The initial nano-sized heterogeneities caused by minor Cu addition is considered to facilitate the rejuvenation process. The internal stress caused by the thermal expansion coefficient difference in the heterogeneous structures leads to the disordering behaviour including the increased amount of loose-packed regions

and the destruction of initial ordering in nano-scale. This study provides a fundamental guideline for composition selection for thermal cycling. However, the complicated structural variation and deformation behaviours suggest that a monotonic picture is incomplete, a more complex structural model with multi-scale and long temporal evolution should be established to accurately predict the deformation behaviour of CTC treated BMGs.

Declaration of Competing Interests

The authors declare that they have no known competing financial interests or personal relationships that could have appeared to influence the work reported in this paper.

References

[1] A. Inoue, Y. Shinohara, J.S. Gook, Mater. Trans. 36 (1995) 1427–1433 JIM.
[2] A. Inoue, B.L. Shen, Adv. Mater. 16 (2004) 2189–2192.
[3] C. Suryanarayana, A. Inoue, Int. Mater. Rev. 58 (2013) 131–166.
[4] M. Stoica, J. Eckert, S. Roth, Z.F. Zhang, L. Schultz, W.H. Wang, Intermetallics 13 (2005) 764–769.
[5] A. Makino, X. Li, K. Yubuta, C. Chang, T. Kubota, A. Inoue, Scr. Mater. 60 (2009) 277–280.
[6] B. Sarac, Y.P. Ivanov, A. Chuvilin, T. Schöberl, M. Stoica, Z. Zhang, J. Eckert, Nat. Commun. 9 (2018) 1333.
[7] Y.H. Liu, G. Wang, R.J. Wang, D.Q. Zhao, M.X. Pan, W.H. Wang, Science 315 (2007) 1385–1388.
[8] S.V. Ketov, Y.H. Sun, S. Nachum, Z. Lu, A. Checchi, A.R. Beraldin, H.Y. Bai, W.H. Wang, D.V. Louzguine-Luzgin, M.A. Carpenter, A.L. Greer, Nature 524 (2015) 200–203.
[9] H. Zheng, L. Zhu, S.S. Jiang, Y.G. Wang, F.G. Chen, J. Alloys Compd. 790 (2019) 529–535.
[10] W.L. Song, X.H. Meng, Y. Wu, D. Cao, H. Wang, X.J. Liu, X.Z. Wang, Z.P. Lu, Sci. Bull. 63 (2018) 840–844.
[11] S.V. Ketov, A.S. Trifonov, Y.P. Ivanov, A.Y. Churyumov, A.V. Lubenchenko, A.A. Batrakov, J. Jiang, D.V. Louzguine-Luzgin, J. Eckert, J. Orava, A.L. Greer, NPG Asia Mater. 10 (2018) 137–145.
[12] W. Guo, J.J. Saida, M. Zhao, S.L. Lü, S.S. Wu, Mater. Lett. 247 (2019) 135–138.
[13] W. Guo, R. Yamada, J. Saida, S. Lu, S. Wu, Nanoscale Res. Lett. 13 (2018) 398.
[14] S. Sohrabi, M.C. Ri, H.Y. Jiang, L. Gu, P. Wen, Y.H. Sun, W.H. Wang, Intermetallics 111 (2019) 106497.
[15] S.Y. Di, Q.Q. Wang, J. Zhou, Y.Y. Shen, J.Q. Li, M.Y. Zhu, K.B. Yin, Q.S. Zeng, L.T. Sun, B.L. Shen, Scr. Mater. 187 (2020) 13–18.
[16] W.F. Wu, Y. Li, C.A. Schuh, Philos. Mag. 88 (2008) 71–89.
[17] Z.F. Zhang, F.F. Wu, G. He, J. Eckert, J. Mater. Sci. Technol. 23 (2007) 747–767.
[18] M. Stoica, J. Eckert, S. Roth, Z.F. Zhang, L. Schultz, W.H. Wang, Intermetallics 13 (2005) 764–769.
[19] S. Lesz, Mater. Charact. 124 (2017) 97–106.
[20] J. Pan, Y.P. Ivanov, W.H. Zhou, Y. Li, A.L. Greer, Nature 578 (2020) 559–562.
[21] H.B. Ke, J.F. Zeng, C.T. Liu, Y. Yang, J. Mater. Sci. Technol. 30 (2014) 560–565.
[22] H. Guo, C.B. Jiang, B.J. Yang, J.Q. Wang, J. Mater. Sci. Technol. 33 (2017) 1272–1277.
[23] G.R. Garrett, M.D. Demetriou, M.E. Launey, W.L. Johnson, Proc. Natl. Acad. Sci. 113 (2016) 10257–10262.
[24] K.-W. Park, C.-M. Lee, M. Wakeda, Y. Shibutani, M.L. Falk, J.-C. Lee, Acta Mater. 56 (2008) 5440–5450.
[25] L. Zhang, Y. Wu, S.D. Feng, W. Li, H.W. Zhang, H.M. Fu, H. Li, Z.W. Zhu, H.F. Zhang, J. Mater. Sci. Technol. 38 (2020) 73–79.
[26] M. Stoica, R. Li A.R. Yavari, G. Vaughan, J. Eckert, N.V. Steenberge, D.R. Romera, J. Alloys Compd. 504 (2010) S123–S128.
[27] B.L. Shen, H. Men, A. Inoue, Appl. Phys. Lett. 89 (2006) 101915.
[28] K. Hono, D.H. Ping, M. Ohnuma, H. Onodear, Acta Mater. 47 (1999) 997–1006.
[29] Q. Hu, J.M. Wang, Y.H. Yan, S. Guo, S.S. Chen, D.P. Lu, J.Z. Zou, X.R. Zeng, Intermetallics 93 (2018) 318–322.
[30] J. Hwang, Z.H. Melgarejo, Y.E. Kalay, I. Kalay, M.J. Kramer, D.S. Stone, P.M. Voyles, Phys. Rev. Lett. 108 (2012) 195505.
[31] C.C. Yuan, Z.W. Lv, C.M. Pang, X.L. Wu, S. Lan, C.Y. Lu, L.G. Wang, H.B. Yu, J.H. Luan, W.W. Zhu, G.L. Zhang, Q. Liu, Xun-Li Wang, B.L. Shen, J. Alloys Compd. 798 (2019) 517–522.
[32] J. Zhou, Q.Q. Wang, X.D. Hui, Q.S. Zeng, Y.W. Xiong, K.B. Yin, B.A. Sun, L.T. Sun, M. Stoica, W.H. Wang, B.L. Shen, Mater. Des. 191 (2020) 108597.
[33] T. Burgess, M. Ferry, Mater. Today 12 (2009) 24–32.
[34] J. Hay, Exp. Tech. 33 (2009) 66–72.

[35] W.C. Oliver, G.M. Pharr, J. Mater. Res. 7 (1992) 1564–1583.
[36] L.S. Luo, B.B. Wang, F.Y. Dong, Y.Q. Su, E.Y. Guo, Y.J. Xu, M.Y. Wang, L. Wang, J.X. Yu, R.O. Ritchie, J.J. Guo, H.Z. Fu, Acta Mater. 171 (2019) 216–230.
[37] J.W. Qiao, J. Mater. Sci. Technol. 29 (2013) 685–701.
[38] Y. Wu, H. Wang, X.J. Liu, X.H. Chen, X.D. Hui, Y. Zhang, Z.P. Lu, J. Mater. Sci. Technol. 30 (2014) 566–575.
[39] M.W. Chen, A. Inoue, W. Zhang, T. Sakurai, Phys. Rev. Lett. 96 (2006) 245502.
[40] E. Bouchaud, D. Boivin, J.L. Pouchou, D. Bonamy, B. Poon, G. Ravichandran, Europhys. Lett. 83 (2008) 66006.
[41] J. Ketkaew, R. Yamada, H. Wang, D. Kuldinow, B.S. Schroers, W. Dmowski, T. Egami, J. Schroers, Acta Mater. 184 (2020) 100–108.